28

STATE RESEARCH CENTER OF RUSSIA
Institute of Theoretical
and Experimental Physics

FERMILAB
SEP 4 1997
LIBRARY

16-97

ITEP-16-97

H. Bokemeyer, P. Finocchiaro, I. Iori, W. Koenig, W. Kühn,
N. Rabin, H. Schön, P. Shishov, V. Smoliankin, V. Ushakov,
D. Vassiliev

The TOFW for the HADES Spectrometer

Fermilab Library
0 1160 0057983 3

Moscow 1997

UDK 539.1 M-16

THE TOFW FOR THE HADES SPECTROMETER: Preprint ITEP 16-97/

H. Bokemeyer[2], P. Finocchiaro[5], I. Iori[4], W. Koenig[2], W. Kühn[3], N. Rabin[1], H. Schön[2], P. Shishov[1], V. Smoliankin[1], V. Ushakov[1], D.Vassiliev[1] - M., 1997 - 26p.

The Time-of-Flight Wall (TOFW) is a part of the Multiplicity Electron Trigger Array (META) destined to supply a first and a second level trigger for the High Acceptance DiElectron Spectrometer (HADES) which is at present under construction at GSI. Here presented are results of simulations of the TOFW as well as analysis of long scintillator counter performance which allow to make conclusions about design and expected performance of the TOFW.

Fig. - 25, ref. - 7 name.

© Институт теоретической и экспериментальной физики, 1997

[1]ITEP Moscow, [2]GSI Darmstadt, [3]Universität Gießen, [4]Univ. and INFN Milano, [5]INFN-LNS Catania

1 Introduction

The HADES spectrometer [1] is designed to study nuclear matter features as well as temperature and density influence of nuclear matter on the properties of particles produced in interactions. ω and ρ mesons have been chosen to be the objects of investigation because a significant fraction of these mesons will decay inside the hot dense reaction zone. The purpose of the HADES spectrometer is to detect dilepton pairs from the decays of ω and ρ mesons. Leptons present a sensitive probe since they do not undergo nuclear interactions and carry undistorted information from the reaction zone. The probability of dilepton decays $\omega, \rho \rightarrow e^+e^-$ is small, $\sim 10^{-5}$, and therefore the problem to get a good signal to background ratio, when one has about 170 protons and charged pions in one event in the central Au + Au collision at 1 GeV/u bombarding energy, becomes very important.

The HADES spectrometer consists of 6 symmetric sectors each covering the range of azimuthal angle $\Delta\phi = 60°$. Fig. 1 shows 2 sectors of the spectrometer, which consists of the following components: a magnet spectrometer, a Cherenkov RICH detector, and META detector, which comprises a scintillator TOF hodoscope and a shower detector. The magnet spectrometer consists of a toroidal magnet and two groups of drift chambers located in front and after the magnet. The spectrometer provides measurement of charged particles momenta with the accuracy $\sigma/p \simeq (1 \div 2)\%$.

The gas Cherenkov detector (RICH) is located just after the target before the magnet spectrometer. It is absolutely not sensitive to pions and protons in the working range of electron momenta < 2 GeV/c. RICH detects electrons with high efficiency, about 95%,

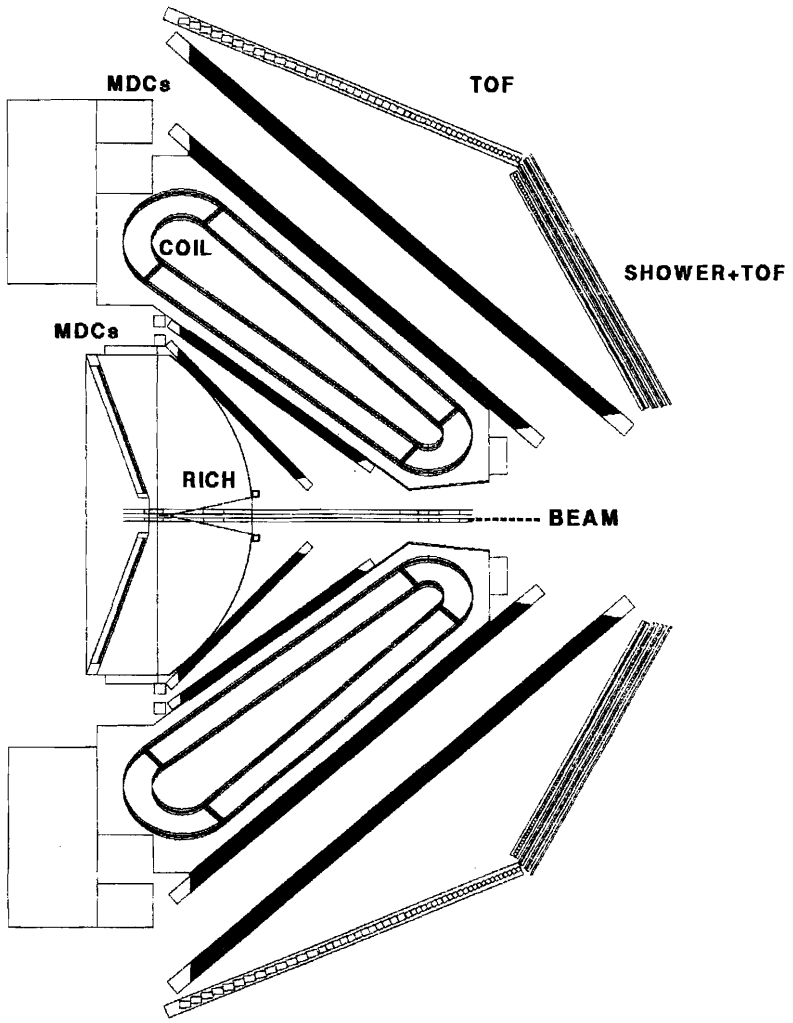

Figure 1: Schematic view of 2 sectors of the HADES spectrometer.

and marks all $e^{\pm}$ tracks that pass then through the magnet spectrometer and META detector. The accuracy of determination of the angle at which electron leaves the target is equal $\sigma \simeq 2.3\, mrad$ in the directions of polar and azimuthal angles.

META detector is located after the magnet spectrometer just after the outermost drift chamber at the distance $L \simeq 220\ cm$ from the target. It consists of the scintillator TOF hodoscope and the shower detector. META must identify electron and determine its location, thus confirming passage of the electron track after the magnet through the area S, defined by the RICH angle resolution. The size of this area in the plane of META detector on the level of 2 $\sigma_{\theta,\phi}$ is about $S_{\theta,\phi} \sim 2.0\ cm^2$. Electron identification in META is based on the particle time-of-flight (TOF) measurement on the length $L \simeq 220\ cm$ by means of the TOF hodoscope and on the electron feature to produce the electromagnetic showers in the shower detector. The TOF hodoscope should be able both to detect electrons by means of TOF and measure the coordinates of electron hit. Besides, the scintillator hodoscope is used to produce the central collision trigger and the second level trigger to select electron events.

Central collisions are defined by charged particles multiplicity measurement. Fig. 2 demonstrates total multiplicity of charged particles, normalised to HADES acceptance, for Au + Au collisions at 1 GeV/u bombarding energy. Fixing the value of the threshold

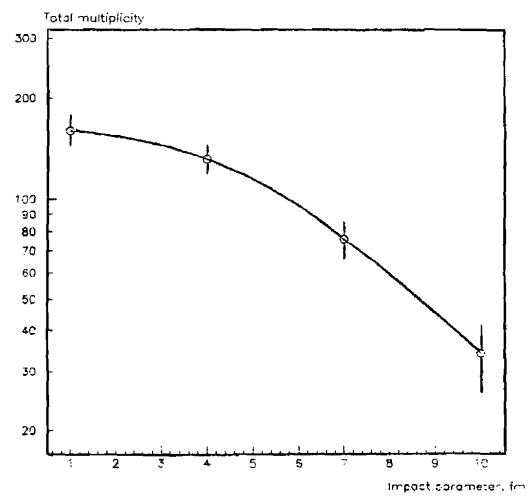

Figure 2: Charged particles multiplicity versus impact parameter is depicted.

multiplicity N_{thr} it is possible to define impact parameter and hence the centrality of Au + Au interaction. If one selects only events that have charged particles multiplicity $N \geq 160$ then a sample of events with impact parameter $< 4\ fm$ is formed. If the accuracy of multiplicity determination gets worse the range of impact parameters will be broadened.

Thus, the TOF hodoscope must

- provide maximum possible hadron rejection with high efficiency, $\geq 90\%$, of electron detection;

- possess sufficient granularity. This is necessary both to obtain the unbiased estimate of the charged particles multiplicity and to reduce the electron losses from double hits. The part of such events should not exceed $\simeq 20\%$.

The task of this paper is to estimate the design of the whole hodoscope and its individual parts. Some of the results which are described here, have been presented at HADES Workshop III in GSI, Darmstadt and HADES Workshop IV in Rez, Czech Republic.

2 Particle Identification

Time-of-flight (TOF) of the particle with mass m and momentum p is given by a relation

$$t = (L/c)(1 + (mc/p)^2)^{1/2} \tag{1}$$

where L is the length of the particle trajectory and c is the velocity of light. Identification is based on different TOF for particles with fixed momentum and masses m_1 and m_2:

$$\delta t = (L/c)((1 + (m_1c/p)^2)^{1/2} - (1 + (m_2c/p)^2)^{1/2}) \tag{2}$$

If σ_i is a standard deviation in TOF distribution t_i then error in δt measurement is equal to

$$\sigma = (\sigma_1^2 + \sigma_2^2)^{1/2} \tag{3}$$

If the value of δt is larger than error, $k = (\delta t/\sigma) > 1$, then it is possible to distinguish particles with the mutual admixture defined by k.

Relation (2) allows to determine the momentum range where it is possible to separate two particles if the values of time resolution, efficiency and mutual admixture are given. The results of calculations for $\sigma = (0.1 \div 1.0)$ ns and $k = 2, 3, 4$ are shown on fig. 3 for the particle pairs electron-proton (a), electron-pion (b) and pion-proton (c). Fig. 4 demonstrates efficiency of single electron detection (a) and hadron admixture (b) as a function of $k = \delta t/\sigma$. It can be seen that for $k = 4$ efficiency is rather high, $\simeq 97\%$ and admixture does not exceed $\simeq 3\%$. The momentum range is defined only by the value of time resolution. If the total resolution amounts to 0.5 ns then the value of the threshold momentum is equal $\simeq 0.25$ GeV for pions and $\simeq 1.7$ GeV for protons. Identification of the pair pion-proton can be effective for the total timing resolution $\sigma \simeq (1 \div 1.5)$ ns and the momentum range $p \leq 1$ GeV.

It is obvious that beginning from the threshold momentum, protons and pions become "dangerous" and can imitate electron signal. Figures 5 and 6 show momentum distributions for pions and protons for 4 different ranges of polar angle θ. Integrating these distributions in the range $\geq p_{thres}$ we obtain the number of "dangerous" hadrons, which can imitate electron. The results for $p_{thres}(k = 2)$ are demonstrated in fig. 7. It can be noticed that for $\sigma \leq 0.2\ ns$ protons are not "dangerous" ($n_p < 1$), but the number of "dangerous" pions is significant ($n_\pi \sim (10 \div 15)$). These "dangerous" pions fly mainly at low polar angles ($\theta < 45°$). For $\sigma = (0.2 \div 0.3)$ ns the number of "dangerous" hadrons increases: for protons up to $n_p \simeq 5$ and for pions up to $n_\pi \simeq (16 \div 20)$.

TOF difference distributions for pions and protons $\delta t = (t_{\pi p} - t_{el})$ have been obtained to define the number of fake electrons. They are shown on fig. 8. The content of each histogramm channel is presented by the normal distribution with dispersion σ^2. The value

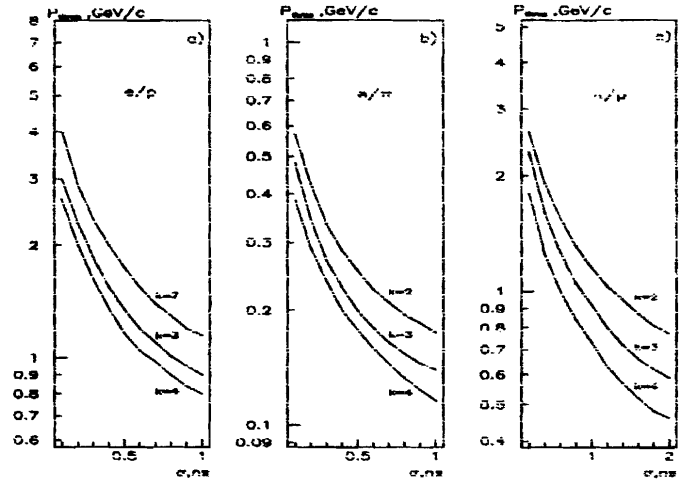

Figure 3: Threshold momentum as a function of time deviation σ a) for protons in case of electron-proton separation; b) for pions in case of electron-pion separation; c) for protons in case of pion-proton separation.

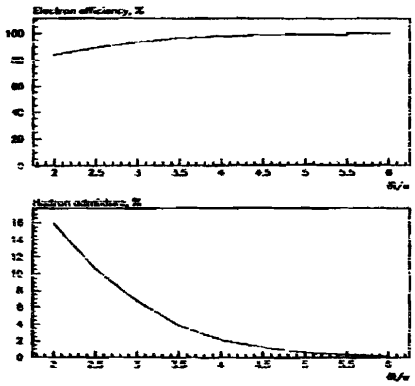

Figure 4: a) single electron detection efficiency; b) hadron admixture versus $\delta t/\sigma$ are depicted.

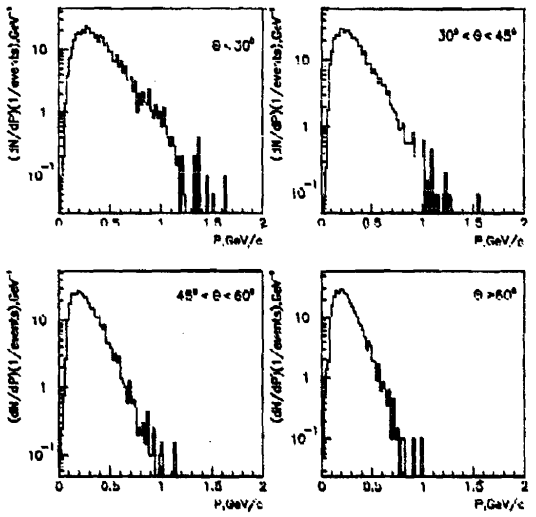

Figure 5: Charged pions momentum distribution for different ranges of polar angle θ.

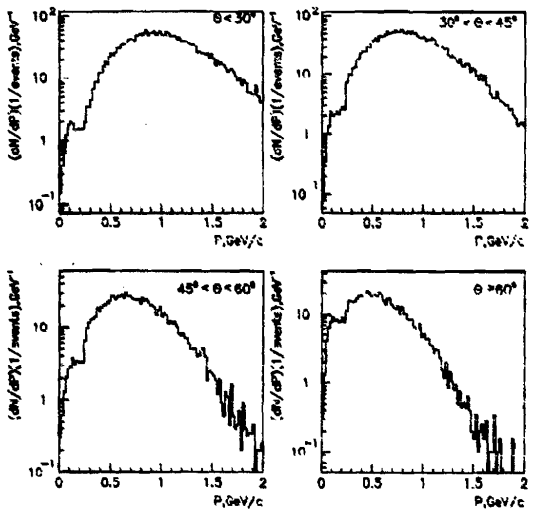

Figure 6: Protons momentum distribution for different ranges of polar angle θ.

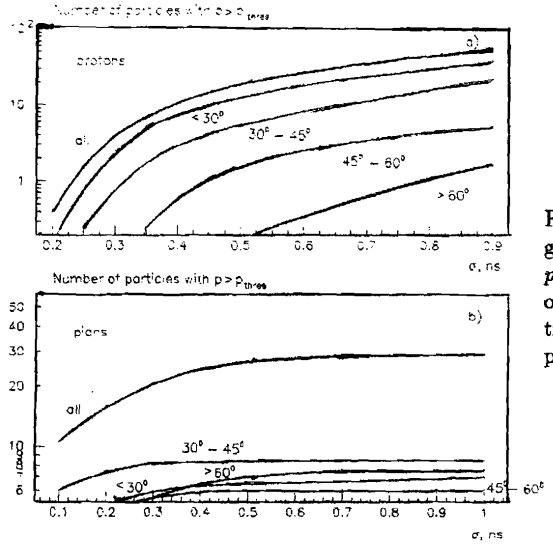

Figure 7: Number of "dangerous" hadrons (with $p > p_{thres}$) for different ranges of polar angle θ as a function of time resolution: a) protons; b) pions.

of the hadron contribution into the region $\delta t \leq 2\sigma$ is calculated. The results of calculation are shown on fig. 9 - 11. The number of fake electrons depends upon the timing resolution. If $\sigma \simeq 0.1 \div 0.2\, ns$ the number of fake electrons is equal $n_{f.el.} \simeq 2 \div 7$. Fake electrons in this case arise only from pions.

It is obvious that electron identification and the number of fake electrons depend upon the total time resolution. It can be seen from the relation (1) that accuracy of the time measurements is defined by

- accuracy of trigger signal which gives the start signal, σ_{tr};
- time resolution of scintillator counters, σ_{sc};
- contribution into the timing resolution of the momentum and trajectory lengths fluctuations, $\sigma(L,p)$.

Dispersion can be presented in the following way

$$\sigma^2 = \sigma_{tr}^2 + \sigma_{sc}^2 + \sigma^2(L,p) \tag{4}$$

$$(\sigma(L,p)/t)^2 = (\sigma_L/L)^2 + ((mc/p)^4/(1 + (mc/p)^2))(\sigma_p/p)^2 \tag{5}$$

Contribution of $\sigma(L,p)$ which happens due to the error in momentum determination $\sigma(p)/p < 2\%$ and to the uncertainty of trajectory length (because of multiple scattering), is not large. It does not exceed $0.02\, ns$ for time-of-flight $\simeq 10\, ns$. This contribution can be neglected. The values of σ_{tr} and σ_{sc} depend on the scintillator counters parameters and will be discussed below.

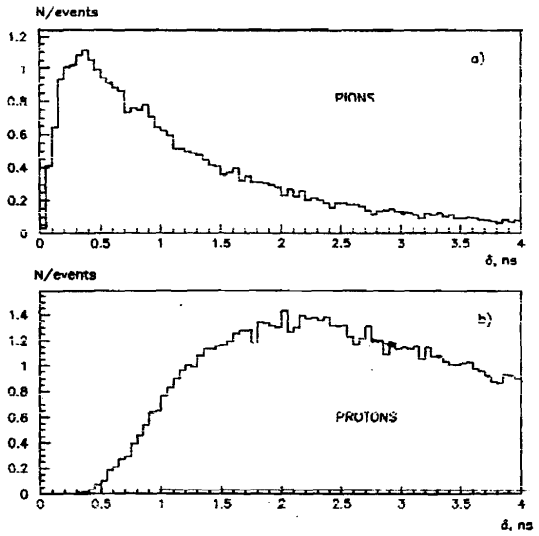

Figure 8: $\delta = t_{sp} - t_{al}$ **distributions: a) for pions; b) for protons.**

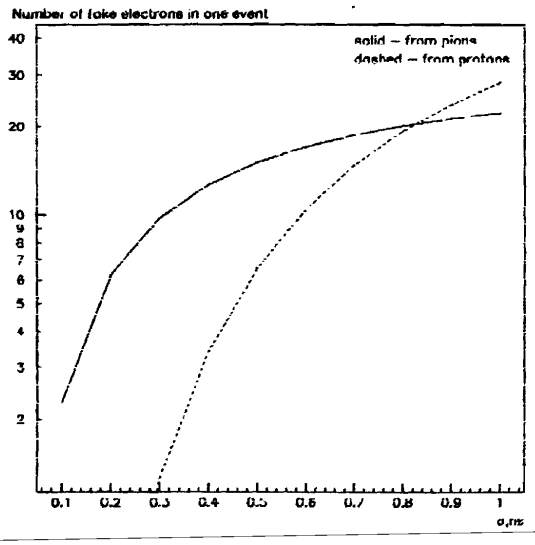

Figure 9: Number of fake electrons versus time resolution is depicted.

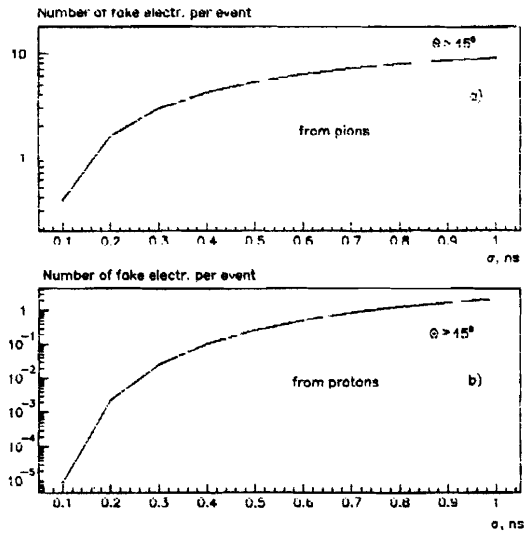

Figure 10: Number of fake electrons at large polar angles ($\theta > 45°$) versus time resolution: a) from pions; b) from protons.

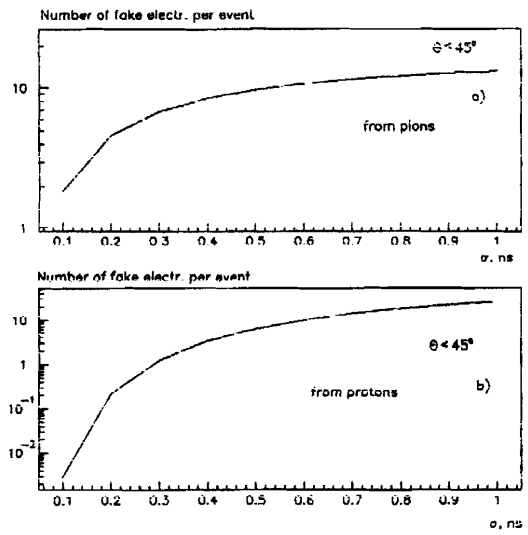

Figure 11: Number of fake electrons at small polar angles ($\theta < 45°$) versus time resolution: a) from pions; b) from protons.

3 Location and Dimensions of Scintillator Hodoscope

The TOF hodoscope consists of 6 planes arranged in the rooms of the toroidal magnet. Each plane covers 60° in the azimuthal direction and the range 13°-87° in the polar direction. The schematic view of the scintillator hodoscope for one sector is shown in fig. 12.a. It consists of two parts, each of trapezoidal form covering polar angles 13°-45° and 45°-87° respectively. Such arrangement of the TOF1 and the TOF2 planes reduces variation of

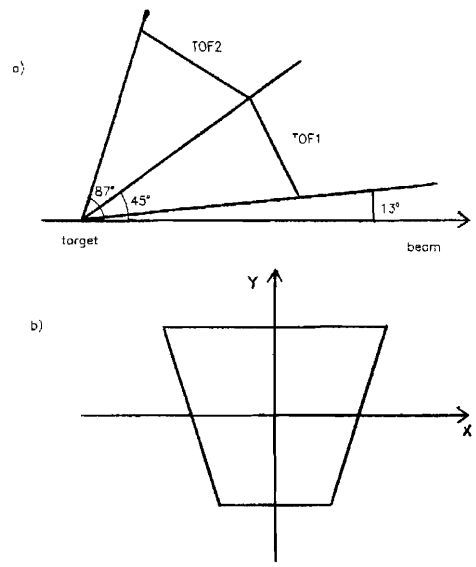

Figure 12: a) schematic view of the TOF planes for one sector; b) one of the trapeziums with intrinsic reference system.

the distance from the target to the scintillator hodoscope in the polar direction. The height of each trapezoidal form in Y-direction (see fig. 12.b) is defined by the range of covered polar angles. It amounts to $H_1 \simeq 125\ cm$ for lower part and to $H_2 \simeq 170\ cm$ for upper one.

Dimensions in X-direction are defined both by the rooms of the magnet and by the values of the shadows from the magnet coils. It is important to know the sizes of the shadows because they provide arrangement of photomultiplier tubes (PMT) and organisation of light transportation. Calculations have been done for 6 ranges of polar angle θ. For each range the number of particles hitting the hodoscope plane versus distance δ from the border of the sector has been determined. The results are shown on fig. 13. These data can be approximated by the linear function

$$\delta = 0.18 \cdot \theta + 5.66 \tag{6}$$

The values of the shadow vary from $\delta \simeq 8\ cm$ at low polar angles ($\theta \simeq 18°$) to $\delta \simeq 20\ cm$ at large polar angles ($\theta \simeq 80°$).

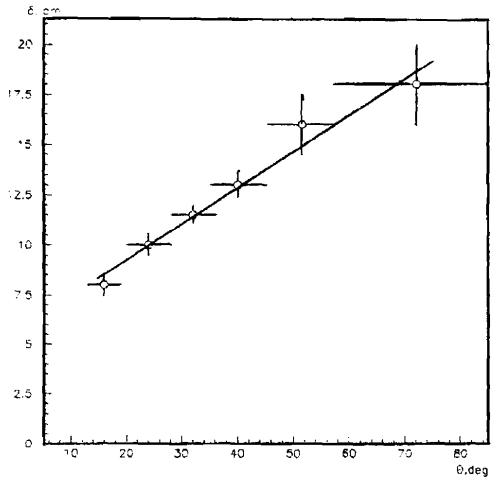

Figure 13: The coil shadow versus polar angle θ is depicted.

4 Counter Design

A scintillator counter is a main part of the TOF hodoscope. Fig. 14 shows the counter and the read-out logic. The counter consists of the scintillator (SC), which is viewed by the photomultipliers PMT1 and PMT2 from both edges. Light transportation from the scintillator to the photocathodes of PMT is carried out by means of the light guides (LG) (or without them), and optical contacts with the photocathode - by means of elastic Sylgard cookie.

Signal from PMT goes to the constant fraction discriminators (CFD) and then to the time-to-digital converter (TDC). The primary trigger signal "open" allows the handling of information and the signal "close" blocks up the channel for the time necessary to process this information.

The measured time t_i includes time-of-flight and the forming time of light impulse on the PMT photocathode $t_{lc,i}$. For the first and the second channels (see fig. 14) they can be written as

$$t_1 = tof + t_{lc,1}(L/2 + x) \tag{7}$$

$$t_2 = tof + t_{lc,2}(L/2 - x) \tag{8}$$

For the ideal surfaces of scintillators total internal reflection ratio is equal to $R_{in} = 1.00$ and relations (7-8) can be rewritten as

$$t_1 = tof + t_{lc,1}(L/2) + t_{lc,1}(x) \tag{9}$$

$$t_2 = tof + t_{lc,2}(L/2) - t_{lc,2}(x) \tag{10}$$

According to these relations (9-10) time difference defines the particle hit location in the scintillator counter:

$$x = V_{gr} \cdot (t_1 - t_2)/2 \tag{11}$$

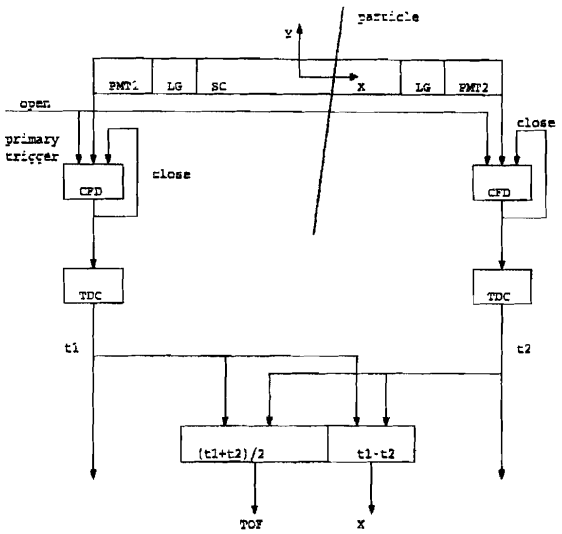

Figure 14: Scheme of the scintillator counter.

V_{gr} here is group velocity of light in the scintillator. Time-of-flight with respect to the scintillator centre is given by a relation:

$$tof = (t_1 + t_2)/2 - (t_{lc,1} + t_{lc,2})/2 \tag{12}$$

It is obvious from the relations (7-12), that procedure of TOF and coordinate measurement requires identity of both measuring channels.

For the bad quality of scintillator surfaces ($R_{in} < 1$) relations (9-10) are not correct and it is possible to obtain the systematic bias in the estimate of tof and x which depends upon the hit location. For the scintillator length $\simeq 1\,m$ asymmetry of the channels on the level $\sim 1\%$ results in the bias of the coordinate estimate about $\sim 1\,cm$, and of the TOF estimate $\sim 50\,ps$.

This means that during the process of the counter production it is necessary to put forward severe requirements to the identity of the channels and to the quality of scintillators.

Time resolution of the counter is defined by

- PMT performance, mainly, the output pulse-rise time and dispersion of electron time-of-flight through the photomultiplier, e.g. the timing jitter;
- number of photoelectrons on the photocathode, e.g. particle energy release in the scintillator and light collection efficiency;
- scintillator features: length, cross section and quality of scintillator surface.

Results of data analysis obtained in time resolution measurements for long scintillator counters [2-3] are given below. We attempt to find out how different factors like scintillator length and cross section, quality of surface and number of photons influence

time resolution. The obtained results allow to make an optimal choice of the scintillator counter design, which defines achievable time and space resolution and counter efficiency.

The counter sizes can be chosen from the following considerations:

- the length is defined by the size of the hodoscope plane and depends upon the possible arrangement of the scintillators: along Y axis or along X axis (see fig. 12.b);
- the thickness is determined by the energy release from the relativistic particle, which provides sufficient statistics of photoelectrons from the PMT photocathode.
- the width is defined by the acceptable value of double-hit probability.

5 Double-Hit Probability

Charged particles multiplicity on the planes of scintillator hodoscope defines the number of double hits and therefore the choice of strip arrangement and granularity of the whole array. Double hit of electron and hadron will result in distortion of time and coordinate information. Electron can be lost. The value of these losses decreases electron detection efficiency.

There are two possible ways to arrange scintillators inside the trapezoidal forms: along X axis and along Y axis (see fig. 12.b). Let us call the first case "horizontal arrangement" and the second one - "vertical arrangement". Geometry which provides the less possible double-hit probability should be chosen.

Fig. 15 demonstrates charged particles (depicted with solid line) total multiplicity for different arrangements of scintillators. The left two pictures on fig. 15 correspond to the vertical arrangement of strips (along Y axis). Multiplicity is presented as a function of the coordinate X integrated over the coordinate Y. On the right two pictures multiplicity is shown as a function of the coordinate Y integrated over the coordinate X. This answers the case when scintillators are arranged along X axis. The upper two pictures correspond to polar angles more than 45°, the lower ones - to polar angles less than 45°. As it can be seen, the most important are the lower parts of scintillator arrays which are located at small polar angles where multiplicities have the highest values. Horizontal arrangement of scintillators (right pictures on fig. 15) is more preferable since it provides the value of double-hit probability about 20% in the maximum. That is better in comparison with vertical case which gives about 25% in the maximum.

It can be seen from fig. 12 that the trajectory length is not the same over the planes of both trapeziums. This inhomogeneity is not large for the lower plane and does not exceed $\sim 5\%$ for the upper one in direction of Y axis (see fig. 12.b). However, in the range of polar angles $45° - 87°$ in direction of X axis inhomogeneity changes significantly from 5% to 15%. If L_c is the length from the target to the center of the strip then for hit with longitudinal coordinate x the length $L(x)$ will be equal to

$$L(x) \simeq L_c \times (1 + (1/2)(x/L_c)^2) \tag{13}$$

All hadrons which hit the strip in the range $x' = 0 \div x$ can reach that strip before electron which hits the strip in point x. These hadrons should have momenta exceeding the values

$$p(x') \geq mc/\delta^2 \tag{14}$$

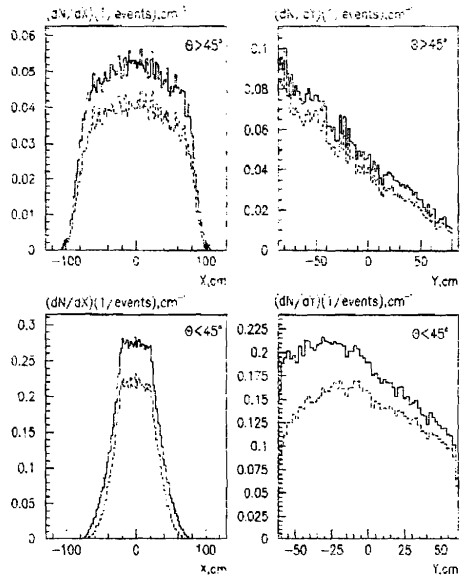

Figure 15: solid line - charged particles multiplicity distributions for vertical (left pictures) and horizontal (right pictures) strip arrangement; dashed line - the same where only particles with $tof < tof_{el} + t_{el,form}(L_{strip})$ are regarded.

where $\delta = (x - x')/L_c$. Such hadrons are "dangerous". But this effect is not essential because multiplicity in the upper planes is not large.

If hadron hits the strip after electron it can become "dangerous" if it reachs the scintillator before electron signal is formed. Time necessary to form electron signal consists of two parts. The first one is time needed for electron to make the way from the target to the TOF wall and the second one is time of light collection in the scintillator $t_{form}(x)$ which depends upon the longitudinal coordinate x of the particle hit on the strip. The maximum value of t_{form} is defined by the full length of the strip. In this case the measured time is equal to

$$t = tof_{el} + t_{form}(L_{strip}) \tag{15}$$

Therefore particles with time-of-flight $tof_x < t$ are "dangerous". All those which have $tof_x > t$ are not detected by the counter because the counter is blocked up when electron signal is handled. Dashed line on fig. 15 shows charged particles multiplicity where only those particles with TOF less than time necessary to handle electron signal are taken into consideration. This effect of multiplicity reduction happens mainly due to slow protons.

Using the results depicted on fig. 15 one can estimate electron detection efficiency as a probability of no hadron hitting the scintillator strip. This value is defined according to the Poisson distribution with the average multiplicity taken from fig. 15 for total multiplicities. It gives the lower limit of electron detection efficiency. In case of horizontal arrangement of scintillator strips the results are shown on fig. 16.

For polar angles $\theta < 45°$ and for the strip width 1 cm efficiency lower limit changes from 80% to 90% with the increase of θ from 20° to 45°.

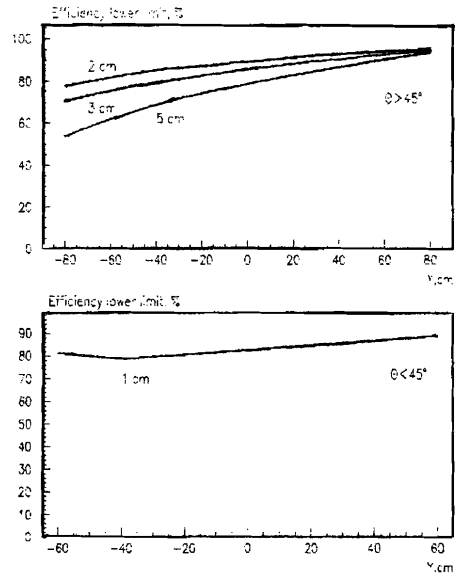

Figure 16: Lower limit of electron detection efficiency versus Y coordinate (horizontal strip arrangement) for different ranges of polar angle θ is depicted. Values 1cm, 2cm etc. on the pictures mark the strip width.

In case of $\theta > 45°$ efficiency lower limits have been calculated for 3 different strip widths: 2, 3 and 5 *cm*. As it follows from fig. 16 it is possible to choose 3 ranges of polar angle (3 ranges of Y in the TOF planes) in which the value of efficiency lower limit will lie within (80 − 90)%.

6 Time Resolution of Scintillator Counters

This section comprises data analysis of time resolution measurements for long scintillator counters presented in [2-3].

Time performance of three types of scintillator counters have been studied with cosmic rays (see tables 1-2).

1. Usual counter assembly - scintillator strip with polished surfaces and aluminium reflector on lateral sides is viewed by photomultipliers:

   - photomultipliers are located at both edges;
   - photomultiplier is located at one edge and the second edge is covered with black paper for light absorption [2-3].

   Photomultiplier tubes (PMT) are coupled with scintillator either directly (C1-C6) or via short, $\sim 20 \div 30$ cm, light guides [2-3].

2. Scintillator strip is covered by a substance with the less refraction ratio, $n = 1.42 \div 1.49$. Thus the structure analogous to that of optical fibre is formed (C10 [2]).

3. Scintillator strip is assembled as a bundle of scintillator fibres (C11 [1]).

Table 1: Performance of Scintillator Counters

Counter	C1	C2	C3	C10	C11
Reference	[1]	[2]	[2]	[2]	[1]
PMT	XP2020	H3284	H3284	H3284	XP2020
QEF	26	20	20	20	26
Light Guide	no	no	no	no	no
K_{lg}	1.	1.	1.	1.	1.
Scintillator	SCSN38	BC404	BC404	BC404	SCSF38
Size, cm	2×3×300	0.8×0.8×100	1.5×1.5×300	1.5×1.5×300	2×3×200
Surface	op	op/poor	op	fibre-structure	fibre-bundle
R_{int}	0.982	0.969	0.992	0.996	0.9999
LY·10^4 phel/MeV	1.24	1.18	1.18	1.18	
N^0_{phel}	738	(280)	(597)	(90)	66
λ, nm		408	408	408	420
t_d, ns	2.7/12.2	1.8	1.8	1.8	2.4
n	1.58	1.58	1.58	1.58	1.59
L^{bulk}_{at}, cm	~ 150	160	160	160	210
$L^{measured}_{at}$, cm	71	25	86	121	182
L_{td}, cm	102±28	49±7	154±6	218±15	316±49
σ_{t0}, ps	69±3	51±5	55±3	79±4	150±9
$\sqrt{N^0_{phel}} \cdot \sigma_{t0}$, ns	1.87	0.85	1.26	0.75	1.22
$\sigma^{cal}_c(tof)$, ps	212	100	103	112	146
$\sigma^{meas}_c(tof)$, ps	204	83	105	114	143

All measurements have been performed according to the scheme shown in fig. 14. As a rule, the start signal is produced by two scintillator counters of small sizes which are located above and below the counter under investigation. Scintillator sizes are chosen to provide reasonable accuracy of the particle hit coordinate measurement and sufficient statistics for reasonable time. Scintillators are viewed by a photomultiplier from one side.

Fig. 17 demonstrates time resolution versus the distance from the particle hit to the PMT photocathode for both photomultipliers. Fig. 18 shows the same data for one photomultiplier [2-3].

Table 2: Performance of Scintillator Counters

Counter	C4	C5	C6
Reference			
PMT	FEU115M	FEU115M	R5600-04
QEF	15*	15*	20
Light Guide	no	yes/direct	no
K_{lg}	1.	0.25	1.
Scintillator	BC408	BC408	BC408
Size, cm	1.5×1.5×150	3×5×220	0.9×0.9×40
Surface	op	op	op
R_{int}	(0.983)	(0.986)	(0.970)
LY·10^4 phel/MeV	1.11	1.11	1.11
N^0_{phel}	(286)	(143)	(260)
λ, nm	425	425	425
t_d, ns	2.1	2.1	2.1
n	1.58	1.58	1.58
L^{bulk}_{at}, cm	380	380	380
$L^{measured}_{at}$, cm	(133)	(162)	(66)
L_{td}, cm	219±30	282±30	111±7
σ_{t0}, ps	90±5	119±7	133±17
$\sqrt{N^0_{phel}} \cdot \sigma_{t0}$, ns	1.52	1.42	2.16
$\sigma^{cal}_c(tof)$, ps	90	124	113
$\sigma^{meas}_c(tof)$, ps	89	126	110

* - this is the average value of QEF at $\lambda = 425\,nm$ obtained by means of data on spectral sensitivity and its uniformity over photocathode area given in [4]

All experimental data can be described by a relation

$$\sigma_t(x) = \sigma_{t0} \cdot exp(x/L_{td}) \tag{16}$$

where L_{td} characterizes degradation of time resolution with increase of the distance from the photocathode, and σ_{t0} is extrapolation of the relation (16) into the point $x = 0$. The results of fitting are shown in tables (1-2).

Analysis of data demonstrated in fig. 17-18 and in tables (1-2) allows to conclude the following.

For the counters 4 and 5 (see fig. 17) there is satisfactory symmetry of both measuring channels. The values of time degradation length are equal to 194±32 cm, 243±50 cm and 289±51 cm, 274±43 cm for the first and the second PMT for the counters 4 and 5. Dispersions σ_{t0} are equal to 88±7 ps, 92±7 ps and 120±10 ps, 117±9 ps respectively. For the counter 6 symmetry is worse: it can be due to the small number of points and not sufficient statistical accuracy. In the following description the average values of L_{td} and σ_{t0} are regarded.

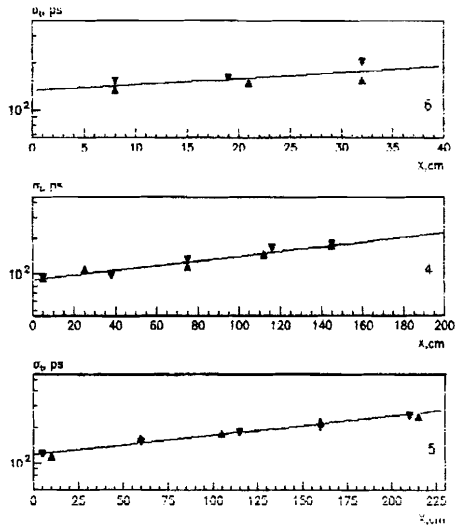

Figure 17: Time resolution versus the distance from the particle hit to the PMT photocathode for two photomultipliers is depicted. Figures 6,4,5 on the pictures mark the counter numbers defined in tables (1-2).

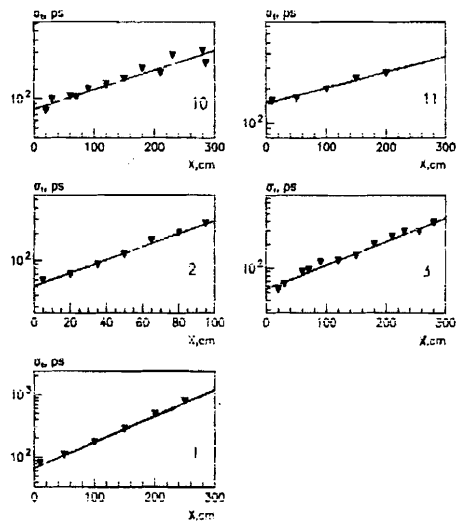

Figure 18: Time resolution versus the distance from the particle hit to the PMT photocathode for one photomultiplier is depicted. Figures 1,2,3 etc. on the pictures mark the counter numbers defined in tables (1-2) [2-3].

It can be seen from the tables (1-2) that the measured value of light absorption length in scintillator strip L_{at}^{meas} is essentially less than this value for a given scintillator material L_{at}^{bulk}. The measured length L_{at}^{meas} is defined by the number of photon reflections from lateral sides and by the full photon path length from the point where it was produced to the photocathode. Thus L_{at}^{meas} depends on the value of total internal reflection ratio R_{int} and on the counter cross section $a \times b$. These values can be described by a relation [2]

$$1/L_{at}^{meas} = 1/(L_{at}^{bulk} \cdot cos\bar{\theta}) + (C/(\pi S))ln(1/R_{int}) \cdot tan\bar{\theta} \qquad (17)$$

In this relation L_{at}^{bulk} is attenuation length of scintillator material, $\bar{\theta}$ is average angle of total internal reflection, R_{int} is total internal reflection ratio, C and S are circumference and area of the scintillator cross section respectively. For adjoining materials with $n_1 = 1$ and $n_2 = 1.58$ $\bar{\theta} = 33°$ and for materials with $n_1 = 1.49$, $n_2 = 1.59$ $\bar{\theta} = 22°$ (for the counters 10, 11). Attenuation length as a function of total internal reflection ratio R_{int} is shown in fig. 19. For scintillator strips 1-6 reflection ratio does not exceed

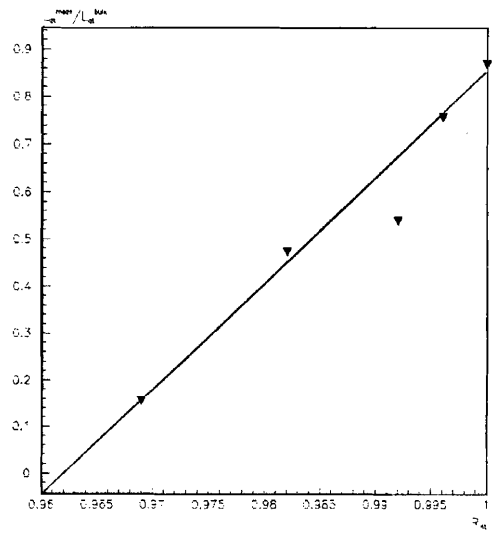

Figure 19: Measured attenuation length in units of L_{at}^{bulk} versus total internal reflection ratio is depicted.

0.98, but for scintillators with fibre-structure ($n_1 \simeq 1.49/n_2 = 1.58$) and fibre-bundle ($n_1 = 1.49/n_2 = 1.59$) it is larger than 0.99. Data on fig. 19 can be approximated by a relation

$$(L_{at}^{meas}/L_{at}^{bulk}) = -0.03 + (R_{int} - 0.96) \cdot 21 \qquad (18)$$

If time resolution is defined only by photoelectron statistics on the PMT photocathode then its dependence upon the distance x from the photocathode can be written in the following way.

$$\sigma_t(x) = \sigma_{t0}/\sqrt{N_{phel}} \qquad (19)$$

$$N_{phel} = N^0_{phel} \cdot exp(-x/L^{meas}_{at}) \tag{20}$$

where

$$N^0_{phel} = LY_{sc}(dE/dx) \cdot \Delta\Omega_{int} \cdot k_{pm} \cdot k_{lg} \cdot t_{sc} \tag{21}$$

Here, LY_{sc}, dE/dx, $\Delta\Omega_{int}$, k_{pm}, k_{lg} and t_{sc} are scintillator light yield, specific energy release, solid angle for total internal reflection angle, photocathode quantum efficiency, light guide transfer ratio, and scintillator thickness along the particle track respectively. From the relation (20) it is possible to receive an expression for degradation length of time resolution

$$L_{td} = 2 \cdot L^{meas}_{at} \tag{22}$$

Fig. 20 demonstrates degradation length L_{td} as a function of measured attenuation length L^{meas}_{at}. Dashed line shows the relation (22). Experimental data can be approximated by

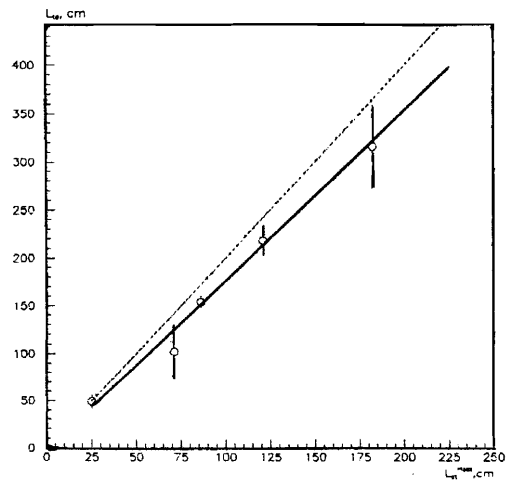

Figure 20: Degradation length versus measured attenuation length is depicted. Dashed line shows theoretical dependence.

the linear function

$$L_{td} = 1.77 \cdot L^{meas}_{at} \tag{23}$$

It points out that time resolution gets worse more significantly with the increase of the distance from the photocathode. This may happen due to light collection [2].

The value of $\sigma_{t0}(x = 0)$ in relation (16) depends upon timing degradation length. These data are shown on fig. 21. They can be approximated by exponential relation

$$\sigma_{t0} = C_1 \cdot exp(L_{td}/C_2) \tag{24}$$

where $C_1 = 38 \pm 5$ and $C_2 = 260 \pm 40$. The value of σ_{t0} is defined only by photoelectron statistics on the photocathode.

$$\sigma_{t0} = \sigma_0/\sqrt{N^0_{phel}} \tag{25}$$

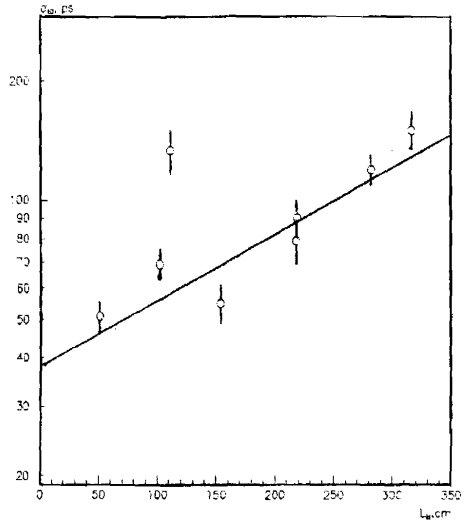

Figure 21: Time resolution extrapolated to the point $x = 0$ versus timing degradation length is depicted.

The estimate of N^0_{phel} has been performed according to the relation (20). The values of N^0_{phel} estimate are shown in tables (1-2) in brackets. For the counters 1 and 11 they have been measured experimentally [1].

In tables (1-2) the values of σ_0 are shown.

$$\sigma_0 = \sigma_{t0} \cdot \sqrt{N^0_{phel}} \tag{26}$$

Within the limits of experimental data errors the value of σ_0 is approximately constant and equal to

$$\sigma_0 = 1.27\, ns \tag{27}$$

It lies in accordance with the value $\sigma_0 = (1.16 \pm 0.12)\, ns$ obtained in [2]. Time resolution related to the centre of the strip can be written in the way

$$\sigma_{tof}(x) = (1/2) \cdot \sqrt{\sigma^2_{t1}(x) + \sigma^2_{t2}(x)} \tag{28}$$

Taking into account the relation (16) we can rewrite it

$$\sigma_{tof}(z) = \sigma_c \cdot \sqrt{cosh(2 \cdot z / L_{td})} \tag{29}$$

where

$$\sigma_c = (1/\sqrt{2}) \cdot \sigma_{t0} \cdot exp(L_{sc}/(2 \cdot L_{td})) \tag{30}$$

$z = x - L_{sc}/2$, where L_{sc} is the length of the scintillator strip. The last two lines of tables (1-2) show calculated $\sigma^{cal}_c(tof)$ and measured $\sigma^{meas}_c(tof)$ values of time resolution in the centre of strip.

Relative time resolution $\sigma_{tof}/\sigma_c(tof)$ versus the particle hit coordinate are shown on fig. 22. Solid line reflects the relation (29). It can be seen that experimental data are in a good accordance with theoretical predictions.

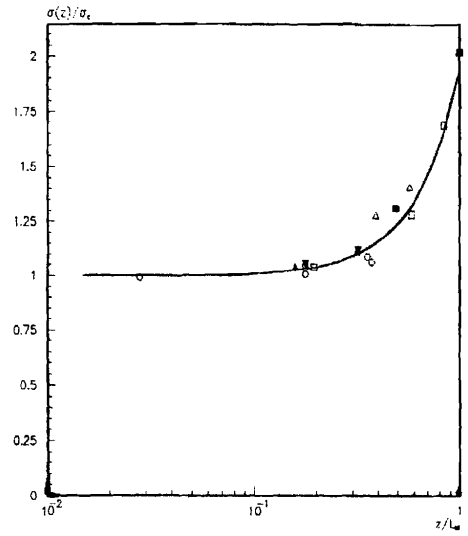

Figure 22: Time resolution in the point z versus hit coordinate expressed in units of degradation length is depicted. Solid line is a theoretical prediction.

7 Longitudinal Coordinate Measurement

Longitudinal coordinate of the particle hit on the scintillator strip is defined by the TOF difference measured by the both photomultipliers, and finally by the difference of light collection time in both channels.

$$x = V_{gr} \cdot (t_1 - t_2)/2 = V_{gr} \cdot (t_{lc,1} - t_{lc,2})/2 \tag{31}$$

V_{gr} can be regarded as the value of light signal "group" velocity in the scintillator. It is defined by the time when the light signal is formed on the photocathode to the level which corresponds the threshold of electronic channel trigger.

If $c' = c/n$ is light velocity in the matter with refraction ratio n and $l_i(z, \vec{p_i})$ is the path length to the photocathode of i-th photon which has left the point z in the direction defined by $\vec{p_i}(\theta_i, \phi_i)$ then its arrival time on the photocathode is equal to

$$t_i = l_i(z, \vec{p_i})/c' \tag{32}$$

Then if probability of that photon to hit the photocathode in the time interval $t, t + dt$ is $W(z,t)\cdot dt$ then timing dependence of the light signal intensity on the photocathode can be presented as a sum of photons hitting successively the photocathode

$$I(t) = \int W(z,t)\cdot dt \tag{33}$$

When the threshold value I_{thr} is reached, electronic channel triggers and detects the measured time $t(I_{thr})$. This time between the moment when the particle hits the strip

and the moment when electronic channel triggers is the light signal formation time on the photocathode, t_{lc}. Together with the distance z to the photocathode it defines the value of group velocity

$$V_{gr} = z/t_{lc} \tag{34}$$

The probability $W(z, \vec{p}, t)$ for the photon to reach PMT in moment t is defined by the matter properties such as light attenuation length L^b_{at} and total internal reflection ratio R_{int}. It is obvious that group velocity is an individual feature of each counter and depends upon light attenuation length L^b_{at}, quality of surface processing R_{int} and properties of electronic channel I_{thr}.

$$V_{gr} = V_{gr}(n, L^b_{at}, R_{int}, I_{thr}) \tag{35}$$

It follows then that parameter V_{gr} should be measured with good accuracy, $\leq 1\,\%$, in test measurements for each counter of the hodoscope.

Results of such measurements for the counter C5 are given below. Fig. 23 depicts time measurements for different distances to the photocathode. It can be seen that

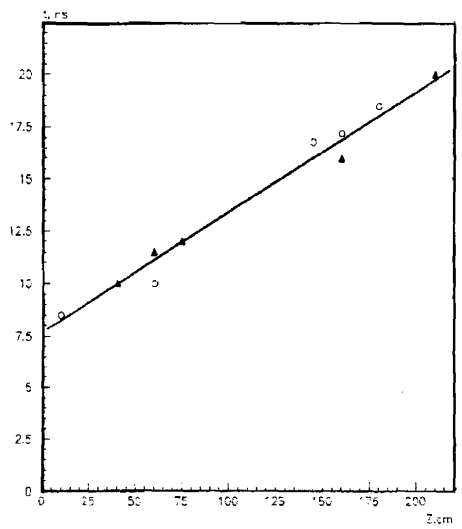

Figure 23: Time versus distance to the photocathode is depicted.

experimental data can be described by a linear relation

$$t = t_0 + z/V_{gr} \tag{36}$$

where $V_{gr} = 17.5 \pm 2.1\ cm/ns$. The value of V_{gr} is close to the estimate which can be obtained from the values of light velocity in scintillator c' and average angle of total internal reflection $\bar{\theta}_{in}(n = 1.6) = 33°$.

$$V_{gr} = c' \cdot cos\bar{\theta}_{in} \simeq 16\ cm/ns \tag{37}$$

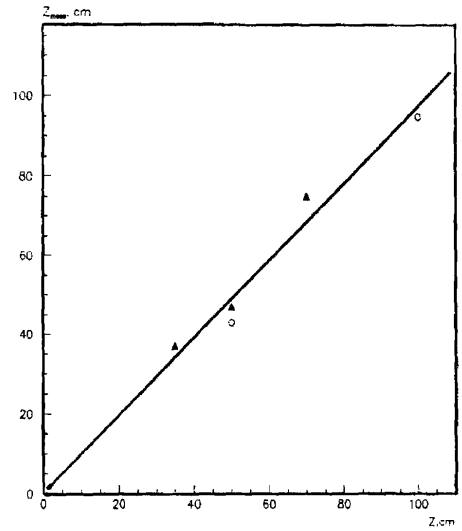

Figure 24: Measured coordinate versus real distance to the photocathode is depicted.

Fig. 24 shows results of gauge curve measurements $z_{meas}(z)$. Data can be described by a linear relation

$$z_{meas} = z_0 + K \cdot z \tag{38}$$

where $z_0 = 0.4 \pm 3.6\ cm$ and $K = 0.97 \pm 0.06$. Unfortunately, accuracy of available data does not allow to put them under detailed discussion.

With respect to accuracy of longitudinal coordinate measurements, it can be described as follows

$$\sigma(z_m, z) = \sigma_c(z_m) \cdot \sqrt{cosh(2 \cdot z / L_{td})} \tag{39}$$

$$\sigma_c(z_m) = V_{gr} \cdot \sigma_c(tof) \tag{40}$$

If $\sigma_c(tof) \simeq (0.10 \div 0.15)\ ns$ then error in the value z_m will be $\sigma(z_m) \simeq (2 \div 3)\ cm$.

It can be noticed in conclusion that for insufficient quality of scintillator surface polishing ($R_{int} < 1$) one can expect systematical bias in the estimate of longitudinal coordinate. According to the preliminary calculations this bias can reach several per cent.

8 Long Time Stability of the Counter Performance

Long time stability of the scintillator counters basic parameters ($\sigma(t)$, L^m_{at}, L_{td}) is an important feature of large multiunit scintillator detectors.

Instability is connected with the aging of scintillator counters and change for the worse of their parameters. There are two basic reasons of the aging. The first one is conditioned by technology and purity of initial material, for example in case of polystyrene the presence

of residual monomer turns out to be essential factor. Experience shows that if its content is less than 0.1 % then performance degradation will be not worse than $\simeq$1 % per year.

The second reason is connected with the quality of scintillator strip surfaces processing. Insufficient processing results in surface overheating and appearance of a lot of rudimentary microcracks. They become apparent on the surface in time as a set of visible microcracks which form the pattern "frost". This reason is above control. It can result both in significant degradation of the scintillator performance and in large variation of parameters between the selected units of detector.

All the said above can be illustrated by experimental data of light attenuation length measurement in scintillator strip, L^m_{at} [5-7], which are shown in table 3. It can be seen that for the different scintillators degradation changes in the broad range from $\simeq$ 1 % to $\simeq$ 20 % per year.

Table 3: Aging of Scintillator Counters

Scintillator	Strip dimensions $cm \times cm \times cm$	Observation time year	L^m_{at} degradation %/year	$L_{at}(t)/L_{at}(0)$ t, year	Ref
SCSN38		$\simeq$5	0.7	$1. - 7.1 \cdot 10^{-3} \cdot t$	[5]
SCSN81	1×20×300	$\simeq$5	4.9	$1. - 4.91 \cdot 10^{-2} \cdot t$	[5]
NE104	5×15×200	8	2.1 *		[6]
NE110	5×15×200	10	7.6 *		[6]
NE114	3×15×300		18.0		[7]

* - in assumption of linear dependence

The standard approach to struggle against these negative factors is to perform measurement and constant control of the values of all basic parameters during the period of the full detector life.

However, there is another way either to decrease significantly or to eliminate wholly the influence of the second reason. This possibility is connected with arrangement of scintillator strip either as a bundle of scintillator optical fibres [2] or as a scintillator covered with material with less refraction ratio [3] (results of testing of the counters C10, C11 are shown in table 1). From these data one can conclude the following. The estimate of total internal reflection ratio gives the values $R_{int} \geq 0.996$. Light attenuation lengths in the material of scintillator L^b_{at} and in the strip L^m_{at} become approximately equal. Scintillator surface protection will favour stability of these values and guarantee both minimal degradation of the counter performance and minimal variation of all parameters between the counters.

It can turn out that arrangement of scintillator strips with fibre-structure will help to solve the problem of the scintillator performance degradation.

9 Trigger

One of the destinations of the TOF hodocsope in the spectrometer HADES is participation in the second level trigger. Since no track information is available on the stage of the trigger formation TOF information can be used in the form of a look-up table where all surface of the TOF wall is divided into segments and for each segment the length of track approximation and time resolution are known. There are two ways to make approximation of a real track. The first one is to approximate with a straight line which connects the center of the target and the particle hit on the scintillator strip. The second one is to build approximated track of two straight lines which cross in the virtual kick plane of the magnet. This plane is located 30 cm below the 3rd MDC. The first line starts in the target center and its direction is given by information from RICH. The second line connects point on the kick plane and the particle hit on the strip.

The difference between the length of a real track and its approximation introduces additional error σ_L which is regarded in total time resolution of the hodoscope. This difference is influenced also by the target segmentation. The target consists of 16 segments and has the full length in the direction of the beam axis $\simeq 4.5\ cm$ ($\pm 2.2\ cm$). If the number of the segment where interaction has happened is not known one has to start all approximation lines from the target center thus increasing the error.

Calculations of the value $\delta t = (\delta L/L) \cdot tof$ have been done for the described above ways of track approximation. Fig. 25 illustrates δt distribution for case of two straight lines approximation. The upper two pictures answer the polar angles $\theta > 45°$, the lower ones - $\theta < 45°$. The left pictures correspond approximation from the target center (segment is not known), the right ones are built in the assumption that the segment where interaction has happened is known. All histogrammes are fitted with normal distribution and dispersion is taken as the error σ_L.

The results of calculations are summarized in table 4. Data are presented for two possible approximations: with a straight line and with two straight lines. The columns σ_{RICH}, σ_{xy} and σ_{tr} take the meanings either "–" or "σ". "–" denotes that angular resolution of RICH, position resolution of TOF and error σ_{tr} which happens due to segmentation of the target are not regarded. "σ" means that these errors are taken into consideration. For RICH angular resolution has been regarded to be $\sigma_{\theta,\phi} = 2.5\,mrad$, for TOF - $\sigma_x = 3\,cm$, σ_y - the width of the scintillator strip. As far as σ_{tr} is concerned it is defined by the total length of the segmented target ($\simeq 4.5\ cm$) and is equal $\sigma_{tr} \simeq 43\ ps$.

It can be concluded that contribution of the error σ_L does not exceed $\simeq 60\ ps$. This means that total time resolution of the TOF hodoscope will be

$$\sigma = \sqrt{\sigma_{sc}^2 + \sigma_L^2} \simeq \sqrt{130^2 + 60^2} \simeq 143\ ps \tag{41}$$

10 % increase of time resolution can result in increase of the number of fake electrons to the value of $\simeq 1$.

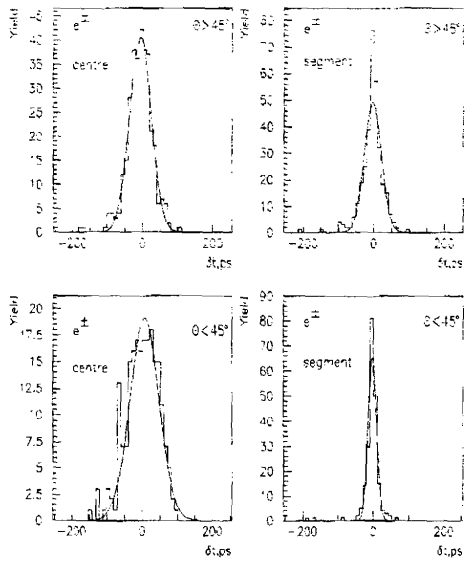

Figure 25: δt distribution in case of track approximation with two straight lines.

Table 4: Contribution of σ_L to TOF Resolution

	Number of segments	σ_{xy}	σ_{RICH}	σ_{tr}	$\sigma_L(\theta \geq 45°), ps$	$\sigma_L(\theta \leq 45°), ps$
Straight line approximation	16	–	–	–	29	43
	16	–	–	σ	52	61
	1	–	–	–	11	8
	16	σ	–	–	33	45
	16	σ	–	σ	54	62
	1	σ	–	–	24	16
Approximation with two straight lines	16	–	–	–	26	42
	16	–	–	σ	50	60
	1	–	–	–	6	5
	16	σ	–	–	32	44
	16	σ	–	σ	54	62
	1	σ	–	–	20	13
	16	σ	σ	–	31	41
	16	σ	σ	σ	53	59
	1	σ	σ	–	24	12

10 Conclusions

The presented data have been obtained by means of analysis

- of the central collisions Au + Au at 1 GeV/u bombarding energy
- and of the results of long scintillator counters time performance measurements [2-3].

The results of this analysis allow to make the following remarks about design and expected performance of the TOF hodoscope.

1. The TOF hodoscope of a selected sector consists of two planes of trapezoidal form covering the ranges of polar angle 13°-45° and 45°-87° respectively.

2. Horizontal (azimuthal) arrangement of scintillator strips with the widths (1.0÷1.5) cm and (2÷5) cm for lower and upper hodoscopes respectively is the optimal choice.

3. Electron detection efficiency is defined by electron identification efficiency and by the number of double hits. Total efficiency of single electron detection lies in the range (80 - 90)%.

4. For the total timing resolution (hodoscope + trigger) $\sigma_t \simeq (150 \div 200)\ ps$ and identification level 95%, number of fake electrons is equal to $n_{fake\,el} \simeq 1 \div 2$ for upper and $n_{fake\,el} \simeq 5 \div 6$ for lower hodoscopes respectively.

5. Required time resolution of individual scintillator counters should not exceed $(100 - 150)\ ps$.

6. The obtained relations define wholly design and timing performance of the counter if its length L_{sc}, required timing resolution in the centre σ_c and admissible resolution change for the worse on the edges of scintillator strip are given. These relations allow to estimate light attenuation length L_{at}^{m}, time degradation length L_{td}, necessary number of photoelectrons N_{phel}^{0} and therefore strip thickness. Timing resolution change for the worse along the strip will not exceed ≃20% if light attenuation length in the strip L_{at}^{m} is at least two times larger than strip length $L_{at}^{m} > 2 \cdot L_{sc}$.

7. Total internal reflection ratio is defined mainly by the quality of scintillator strip surface. That is why counter performance, timing and position resolution are individual features of the selected counter. They should be determined in test measurements.

8. Scintillator performance: light output N_{phel}^{0}, light attenuation length L_{at}^{m} and time degradation length L_{td} change in time due to the process of scintillator aging. It is necessary to have control system for continuous monitoring of counter performance.

REFERENCES

[1] "High-Acceptance Di-Electron Spectrometer" Proposal, GSI, 1994
[2] M.Kühlen et al., Nucl. Instr. and Meth. 1991. A301. P.223
[3] M.Kurata et al., Nucl. Instr. and Meth. 1994. A349. P.447
[4] S.A.Belyanchenko et al., Pr. IHEP 35-12, submitted to NIM
[5] T.Hasegama et al., Nucl. Instr. and Meth. 1992. A311. P.498
[6] N.Grion et al., Nucl. Instr. and Meth. 1986. A251. P.53
[7] A.Diddens et al., Nucl. Instr. and Meth. 1980. 178. P.27

Н.Рабин и др.

Время-пролетный годоскоп для спектрометра ХАДЕС.

Подписано к печати 28.03.97 Формат 60x90 I/I6 Офсетн.печ.
Усл.-печ.л.I,75. Уч.-изд.л.I,3. Тираж 93 экз. Заказ I6.
Индекс 3649

Отпечатано в ИТЭФ, II7259, Москва, Б.Черемушкинская, 25